Dynamical polarization function and plasmons in monolayer XSe (X = In, Ga)

Ma Zhou

BAQIS, Beijing Academy of Quantum Information Sciences, P. O. Box 912, Beijing 100083, China
and SKLSM, Institute of Semiconductors, Chinese Academy of Sciences, P. O. Box 912, Beijing 100083, China

(Received 17 February 2021; revised 13 April 2021; accepted 13 April 2021; published 27 April 2021)

By using the single-band and multiband effective Hamiltonian for monolayer XSe (X=In,Ga), we calculate the density-density response function of monolayer XSe (X=In,Ga) and study its plasmon dispersion within the random-phase approximation. At long wavelengths ($q \to 0$), plasmon dispersion shows the local classical behavior $\omega = \omega_0\sqrt{q}$. Although, monolayer XSe (X=In,Ga) has a nonparabolic "Mexican hat" topmost valence band dispersion which is so different from the parabolic band structure in two-dimensional electron gas, the corresponding density dependence of the plasmon energy is still of the form $\omega_0 \propto \sqrt{n}$ (n is the carrier concentration) as in a conventional two-dimensional electron gas (2DEGs). However, the Fermi energy ($|\mu|$) dependence of the plasmon energy is of the form $\omega_0 \propto |\mu|^{1/4}$, which is different from the conventional 2DEGs ($\omega_0 \propto \sqrt{|\mu|}$).

DOI: 10.1103/PhysRevB.103.155429

I. INTRODUCTION

The dynamical dielectric function and collective density oscillations (plasmons) of electron gas are of fundamental interest from both an experimental and theoretical perspective. Many theoretical [1–3] and experimental [4,5] studies of the dielectric function of various two-dimensional (2D) systems have been made in the past years. The 2D plasmon dispersion relation was first derived by Ritchie [6] and Ferrell [7], who were treating the characteristic energy loss of electrons in metal foils. In 1967, the response of a two-dimensional electron gas (2DEG) to a longitudinal electric field of arbitrary wave vector (q) and frequency (ω) was calculated in the self-consistent-field approximation by Stern [8]. In 1975, 2D plasmons and electron-ripplon scattering in a sheet of electrons on liquid helium was observed by Grimes and Adams [9]. The 2D plasmons also have been experimentally observed in different kinds of 2D systems such as a quantum well [10,11] and metal film [12–16].

All these works indicate that the long-wavelength ($q \to 0$) plasmon dispersion shows the local classical behavior $\omega = \omega_0\sqrt{q}$, and the density dependence of the plasmon energy $\omega_0 \propto n^{1/2}$, where n stands for carrier concentration. This simple relationship between the long-wavelength plasmon energy and carrier concentration ($\omega_0 \propto n^{1/2}$) is a general rule for 2D systems with parabolic band structure. Furthermore, the Fermi energy ($|\mu|$) dependence of the plasmon energy is of the form $\omega_0 \propto \sqrt{|\mu|}$ in 2DEGs.

Since the discovery of graphene in 2004, the linear band structure and corresponding dielectric properties (polarizability, plasmons, and screening) have attracted the attention of many researchers [17]. In 2007, the dynamical dielectric function $\varepsilon(\omega, q)$ of 2D graphene at arbitrary wave vector q and frequency ω is calculated in the framework of the random-phase approximation (RPA) by Hwang and Das Sarma [18]. They conclude that at long wavelengths ($q \to 0$), the plasmon dispersion shows the local classical behavior $\omega = \omega_0\sqrt{q}$, but the density dependence of the plasmon energy ($\omega_0 \propto n^{1/4}$) is different from the usual 2D electron system ($\omega_0 \propto n^{1/2}$) [9]. In 2010, this special density dependence of the plasmon energy was confirmed experimentally by Brar [19]. In spite of the special dependence between plasmon energy and density, the Fermi energy dependence of the plasma energy is of the form $\omega_0 \propto \sqrt{|\mu|}$, which is the same as the form revealed in conventional 2DEGs. Besides graphene, the dielectric properties and plasmon have also been studied in many monolayer materials (such as silicene [20] and MoS_2 [21]). However, the density dependence of the plasmon energy in these 2D materials (silicene [20] and MoS_2 [21]) is all of the form $\omega_0 \propto n^{1/2}$ as in 2DEGs, due to their parabolic band structure.

Recently, the metal monochalcogenide monolayers InSe and GaSe have been successfully synthesized [22]. First-principles calculations and experimental results reveal an unusual nonparabolic topmost valence band (sometimes called a "Mexican hat") [23–25]. Therefore, the nonparabolic valence band structure impact on optical and spin transport properties has attracted the attention of many researchers [26,27]. Here, we investigate the polarization function and the plasmon spectrum in a monolayer XSe (X=In,Ga) by using the $\mathbf{k}\cdot\mathbf{p}$ model Hamiltonian [28]. We show that the location of the plasmon branch in (q, ω) space is strongly dependent on the doping type and strength. In spite of the nonparabolic Mexican hat topmost valence band in monolayer XSe (X=In,Ga), the corresponding density dependence of the plasmon energy is still of the form $\omega_0 \propto \sqrt{n}$ (n represents hole density) as in a 2DEG [8]. However, the Mexican hat topmost valence band leads to a special dependence between the Fermi energy $|\mu|$ and plasmon energy ω_0, which is of the form $\omega_0 \propto |\mu|^{1/4}$. This breaks the law between the Fermi energy and plasmon energy ($\omega_0 \propto \sqrt{|\mu|}$), which is correct in all 2D systems (such as quantum well, graphene, monolayer MoS_2, and so on).

The rest of this paper is organized as follows. In Sec. II, we introduce the $\mathbf{k}\cdot\mathbf{p}$ Hamiltonian for monolayer XSe (X=In,Ga) which can well describe the nonparabolic valence band dispersion. In Sec. III A, we adopt the single-band and multiband $\mathbf{k}\cdot\mathbf{p}$ Hamiltonian to analytically and numerically calculate the polarization function and plasmon dispersion for the hole-doped monolayer XSe (X=In,Ga) base on the RPA method. In Sec. III B, we calculate the polarization function and plasmon for the monolayer InSe monolayer XSe (X=In,Ga) in the electron-doping case. In Sec. IV, we discuss the possible experimental setup which can be used to observe the theoretical results. The summary and final conclusions are in Sec. V.

II. THE MODEL

By adopting the standard invariant theory, the $\mathbf{k}\cdot\mathbf{p}$ Hamiltonian for the XSe (X = In,Ga) monolayer with the D_{3h} point group in the absence of spin-orbit coupling effects can be written as [28]

$$\mathbf{H}_{\mathbf{k}\cdot\mathbf{p}}=\mathrm{diag}\{E_1^c, E_1^v, E_6^v, E_6^v, E_4^c, E_5^v, E_5^v\}+\mathrm{diag}\{\mathbf{H}^{\mathrm{e-e}}, \mathbf{H}^{\mathrm{o-o}}\}, \tag{1}$$

where $E_1^c, \ldots, E_5^v$ are band-edge energies, and

$$\mathbf{H}^{\mathrm{e-e}}=\begin{bmatrix} Fk^2 & b_{11}^{vc}k^2 & ib_{61}^{vc}k_x & ib_{61}^{vc}k_y \\ & Mk^2 & ib_{61}^{vv}k_x & ib_{61}^{vv}k_y \\ & & Ck^2+D(k_y^2-k_x^2) & -2Dk_xk_y \\ & & & Ck^2-D(k_y^2-k_x^2) \end{bmatrix}, \tag{2}$$

$$\mathbf{H}^{\mathrm{o-o}}=\begin{bmatrix} Gk^2 & ib_{54}^{vc}k_x & ib_{54}^{vc}k_y \\ & Ak^2+B(k_y^2-k_x^2) & -2Bk_xk_y \\ & & Ak^2-B(k_y^2-k_x^2) \end{bmatrix}. \tag{3}$$

In the above, we only keep the lowest-order contribution to each matrix element, and only give the matrix elements in the upper triangle since the $\mathbf{k}\cdot\mathbf{p}$ Hamiltonian is Hermitian. It is worth noting that the coupling $\mathbf{H}^{e-o}=(\mathbf{H}^{o-e})^{\dagger}$ between the even-parity and odd-parity states under the mirror reflection vanishes to all orders of k. Therefore, we can safely decouple the Hamiltonian into two parts: $\mathbf{H}^{e-e}$ and $\mathbf{H}^{o-o}$. All the parameters in the Hamiltonian $\mathbf{H}_{\mathbf{k}\cdot\mathbf{p}}$ have already been obtained in Ref. [28].

Base on the above multiband $\mathbf{k}\cdot\mathbf{p}$ Hamiltonian, we display the numerically calculated InSe topmost valence band structure in Fig. 1(a). Figure 1(b) displays the corresponding density of states,

$$D(\mu)=\int\frac{d^2k}{(2\pi)^2}\delta[\mu-E(\mathbf{k})]. \tag{4}$$

As we can see in Fig. 1(a), the Mexican hat band structure leads to two Fermi wave vectors $\mathbf{k}_{F_1}$ and $\mathbf{k}_{F_2}$ for the hole-doping case. For the electron-doping case, the parabolic electron band structure only has one Fermi wave vector $\mathbf{k}_F$ near the bottom of the conduction band, shown in the green inset of Fig. 1(b). More importantly, the red (blue) bands shown in the green inset of Fig. 1(b) stands for even- (odd)-parity bands. In the absence of spin-orbit coupling, we can separately calculate the red and blue bands by using Hamiltonians $\mathbf{H}^{e-e}$ and $\mathbf{H}^{o-o}$.

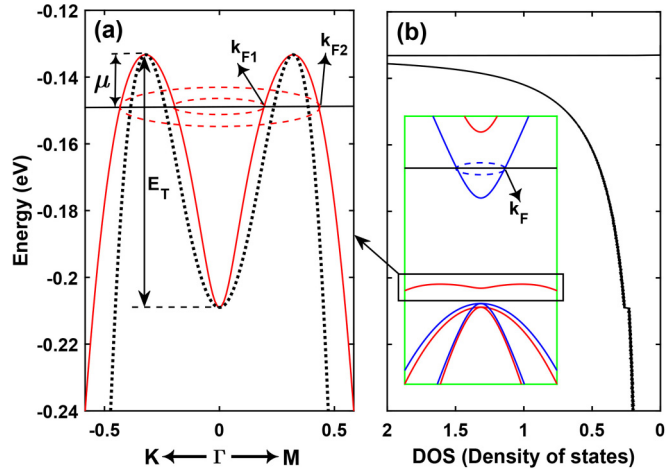

FIG. 1. (a) Topmost valence band structure of monolayer InSe obtained from the multiband $\mathbf{k}\cdot\mathbf{p}$ Hamiltonian (red solid line) and single-band model (black dotted line). The two concentric rings (red dashed) show the two Fermi circles that exist for a definite Fermi energy (black horizontal line). (b) Density of states calculated from the multiband $\mathbf{k}\cdot\mathbf{p}$ Hamiltonian. The peak is located at the upper boundaries of the valence bands (top of the Mexican hat). The green inset shows the whole band structure.

III. POLARIZATION FUNCTION: $\Pi(\omega, q)$

Many physical properties rely on the dynamical dielectric function $\varepsilon(\omega, q)$. In the random-phase approximation (RPA), the dielectric function $\varepsilon(\omega, q)$ is given by [20]

$$\varepsilon(\omega, q)=1-V(q)\Pi(\omega, q). \tag{5}$$

Here, $V(q)=\frac{e^2}{2\epsilon_0\epsilon_r q}$ is the Fourier transform of the Coulomb potential in two dimensions, $V(r)=\frac{e^2}{4\pi\epsilon_0\epsilon_r r}$, ϵ_0 the vacuum permittivity, and $\epsilon_r=5$ the background dielectric constant (comparable to the values in Refs. [29] and [30]). In this paper, all the numerical results are calculated by $\epsilon_r=5$ unless the ϵ_r have been redefined. Equation (5) contains the free polarizability given by a two-dimensional integral in momentum space [21],

$$\Pi(\omega, q)=\sum_{\sigma}\int\frac{d^2k}{(2\pi)^2}|\langle\,\Psi_{\sigma}(\mathbf{k})\mid\Psi_{\sigma'}(\mathbf{k}+\mathbf{q})\,\rangle|^2 \times\frac{f[E_{\sigma}(\mathbf{k})]-f[E_{\sigma'}(\mathbf{k}+\mathbf{q})]}{\omega-E_{\sigma'}(\mathbf{k}+\mathbf{q})+E_{\sigma}(\mathbf{k})+i\,0^+}, \tag{6}$$

where $|\Psi_{\sigma}(\mathbf{k})\rangle$ and $E_{\sigma}(\mathbf{k})$ are the eigenstates and energies, and σ and σ' denote the band indices. Here, we work at zero temperature so that the Fermi functions $f[E_{\sigma}(\mathbf{k})]$ can be replaced by step functions. Notice that only the sum over states with the same even or odd parity appears in Eq. (6), as parity changing transitions are forbidden. Therefore, we only adopt the even- (odd)-parity Hamiltonian given by Eq. (2) [Eq. (3)] to calculate the eigenstates and energies in Eq. (6).

Practically, the imaginary part $\mathrm{Im}[\Pi(\omega, q)]$ of the polarization shown in Eq. (6) is calculated by using the Dirac identity $\mathrm{Im}\{1/(x\pm i0)\}=\mp\pi\delta(x)$ [21]. After the imaginary part of the polarization calculation, the real part of the polarization

can be obtained with the help of the Kramers-Kronig relation,

$$\mathrm{Re}\Pi(\omega, q) = \frac{2}{\pi}\mathbf{P}\int_0^\infty d\omega' \frac{\omega' \mathrm{Im}\Pi(\omega', q)}{\omega'^2 - \omega^2}. \tag{7}$$

Although the multiband Hamiltonians [Eqs. (2) and (3)] can well describe the electronic structure, the analytical results can only be obtained by using the single-band Hamiltonian, which can be used to describe the electronic states near the valence band maximum or conduction band minimum. Base on the single-band model, the polarization function shown in Eq. (6) can be simplified into a Lindhard model,

$$\Pi(\omega, q) = \int \frac{d^2k}{(2\pi)^2} \frac{f[E_\tau(\mathbf{k})] - f[E_\tau(\mathbf{k}+\mathbf{q})]}{\omega - E_\tau(\mathbf{k}+\mathbf{q}) + E_\tau(\mathbf{k}) + i\,0^+}, \tag{8}$$

where the $E_\tau(\mathbf{k}) = E_h(\mathbf{k})$ or $E_\tau(\mathbf{k}) = E_e(\mathbf{k})$ represent the single-band model for the valence band or conduction band.

A. RPA results for hole-doping case

In order to describe the topmost nonparabolic valence band, we develop a higher-order single-band model,

$$E_h(\mathbf{k}) = h_1\mathbf{k}^2 + h_2\mathbf{k}^4 - E_T,\ E_T = -\frac{h_1^2}{4h_2}, \tag{9}$$

where h_1 (h_2) is positive (negative) and E_T represent the energy difference between the valence band maximum states and the topmost valence state at the Γ point. For the Mexican hat band structure [black dotted line shown in Fig. 1(a)], $h_1 = 1.478$ eV Å^2, $h_2 = -7.219$ eV Å^4, and $E_T = 75.7$ meV. Here, we define the energy value corresponding to the valence band maximum to be zero. As we can see, the nonparabolic band structure calculated using Eq. (9) [dotted black line in Fig. 1(a)] is in agreement with the band structure obtained by diagonalizing the multiband Hamiltonian [red solid line in Fig. 1(a)]. By using the single-band model shown in Eq. (9) [$E_h(\mathbf{k})$], we can derive the long-wavelength polarizability $\mathrm{Re}\Pi(q \to 0^+, \omega)$ and plasmon spectrum for the hole-doped XSe (X = In, Ga) monolayer in the framework of the Lindhard model [Eq. (8)].

Under the long-wavelength limit $q \to 0^+$, the Lindhard model shown in Eq. (8) can be simplified to

$$\begin{aligned}\Pi(q \to 0^+, \omega) &= \frac{1}{4\pi^2}\int d^2k \frac{-\mathbf{q}\cdot\nabla f[E_h(\mathbf{k})]}{\omega - \mathbf{q}\cdot\nabla E_h(\mathbf{k})} \\ &\approx -\frac{1}{4\pi^2\omega}\int d^2k \Bigg(\left\{q_x\frac{\partial f[E_h(\mathbf{k})]}{\partial k_x} + q_y\frac{\partial f[E_h(\mathbf{k})]}{\partial k_y}\right\} \\ &\quad + \frac{2}{\omega}(q_xk_x + q_yk_y)(h_1 + 2h_2k^2)\left\{q_x\frac{\partial f[E_h(\mathbf{k})]}{\partial k_x} + q_y\frac{\partial f[E_h(\mathbf{k})]}{\partial k_y}\right\}\Bigg).\end{aligned} \tag{10}$$

In above equation, we have

$$\begin{aligned}\int d^2k \ldots \frac{\partial f[E_h(\mathbf{k})]}{\partial k_x} &= \int d^2k \ldots \frac{\partial f[E_h(\mathbf{k})]}{\partial E_h(\mathbf{k})}\frac{\partial E_h(\mathbf{k})}{\partial k_x} \\ &= 2\int d^2k \ldots \delta[\mu - E_h(\mathbf{k})](h_1 + 2h_2k^2)k_x \\ &= 2\int_0^\infty \delta[\mu - E_h(k)](h_1 + 2h_2k^2)k^2 \ldots dk \int_0^{2\pi} d\theta \ldots \cos\theta\end{aligned} \tag{11}$$

and

$$\int d^2k \ldots \frac{\partial f[E_h(\mathbf{k})]}{\partial k_y} = 2\int_0^\infty \delta[\mu - E_h(k)](h_1 + 2h_2k^2)k^2 \ldots dk \int_0^{2\pi} d\theta \ldots \sin\theta, \tag{12}$$

where, μ stands for the Fermi energy shown by the black horizontal line in Fig. 1(a). By substituting Eqs. (11) and (12) into Eq. (10), we obtain that the first term shown in Eq. (10) equals zero, $\int d^2k\{q_x\frac{\partial f[E_h(\mathbf{k})]}{\partial k_x} + q_y\frac{\partial f[E_h(\mathbf{k})]}{\partial k_y}\} = 0$, and the integrated results are

$$\Pi(q \to 0^+, \omega) = \frac{q^2}{4\pi\omega^2}\frac{h_1\sqrt{4h_2\mu}}{-h_2}. \tag{13}$$

Here, $-\sqrt{4h_2\mu}/h_2 = n$ is the hole concentration corresponding to the Fermi energy μ, where μ is negative for the hole-doping case.

Since the plasmon branch can be obtained by finding the zeros of the dielectric function $\varepsilon(\omega, q)$ [shown in Eq. (5)], we obtain the long-wavelength plasmon spectrum as

$$\begin{aligned}\omega &= \omega_0\sqrt{q} \\ &= \sqrt{\frac{e^2}{8\pi\epsilon_0\epsilon_r}}2(E_T|\mu|)^{1/4}\sqrt{q} = \sqrt{\frac{e^2}{8\pi\epsilon_0\epsilon_r}}\sqrt{h_1}\sqrt{n}\sqrt{q}.\end{aligned} \tag{14}$$

It is worth noting that for the hole-doped monolayer XSe (X = In, Ga), the long-wavelength plasmon spectrum still

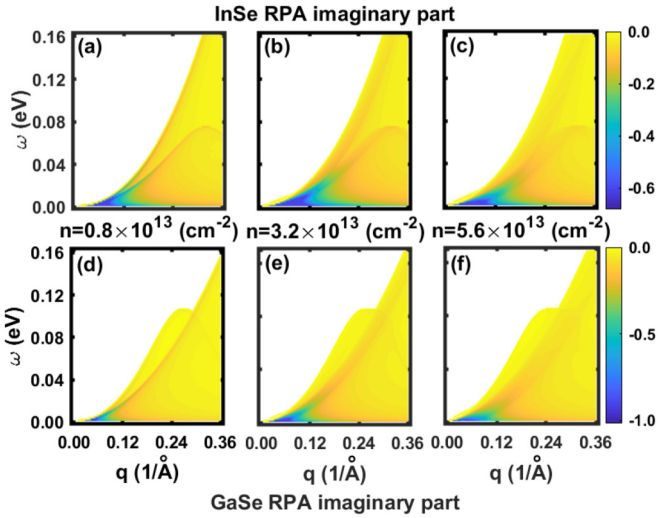

FIG. 2. Imaginary part of the polarization function, $\mathrm{Im}[\Pi(\omega, q)]$, for different carrier concentrations: (a) [(d)] $n = 8 \times 10^{12}$ cm^{-2}, (b) [(e)] $n = 32 \times 10^{12}$ cm^{-2}, and (c) [(f)] $n = 56 \times 10^{12}$ cm^{-2}, in hole-doped InSe [GaSe].

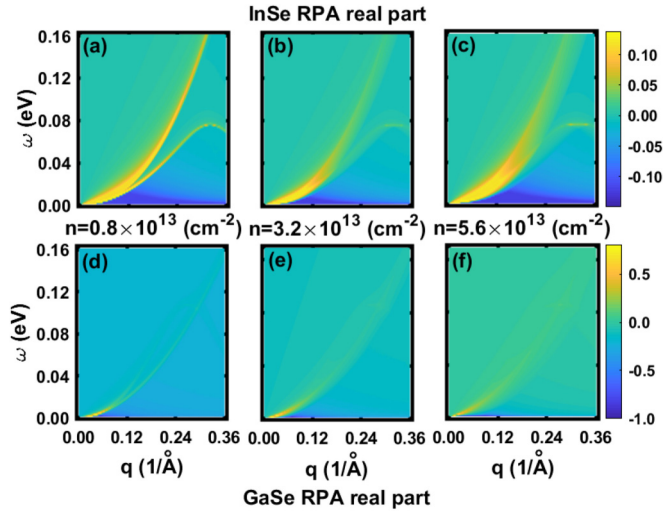

FIG. 3. Real part of the polarization function, $\mathrm{Re}[\Pi(\omega, q)]$, for different carrier concentrations: (a) [(d)] $n = 8 \times 10^{12}$ cm^{-2}, (b) [(e)] $n = 32 \times 10^{12}$ cm^{-2}, and (c) [(f)] $n = 56 \times 10^{12}$ cm^{-2}, in hole-doped InSe [GaSe].

relies on the hole concentration as $\sqrt{n}$, which has the same form as in 2DEGs or other parabolic band structure systems. However, the dependence between the Fermi energy μ and hole concentration n is of the form $n \propto \sqrt{|\mu|}$, which gives rise to a special relation between the plasmon energy ω_0 and Fermi energy $|\mu|$ as the form $\omega_0 \propto |\mu|^{1/4}$.

Next, we recalculate the polarization function and the corresponding plasmon spectrum by adopting the RPA equation (6) in which the needed eigenstates and eigenvalues are obtained by numerically diagonalizing the multiband $\mathbf{k} \cdot \mathbf{p}$ Hamiltonian shown in Eq. (2). We obtain the $\mathrm{Im}[\Pi(\omega, q)]$ for the hole-doped InSe and GaSe monolayer, and display the results on the top and bottom rows in Fig. 2. The imaginary part of the polarization function plays an important role in determining the behavior of the plasmons. As we can see in Fig. 2, the imaginary part of polarization function $\mathrm{Im}[\Pi(\omega, q)] == 0$ in the white space. The white space in Fig. 2 corresponds to values of q and ω for which there is no damping of a collective charge oscillation (undamped plasmon). And the yellow region ($\mathrm{Im}[\Pi(\omega, q)] \neq 0$) in Fig. 2 corresponds to regions in which collective oscillations are damped (damped plasmon). Besides plasmons, the particle hole excitation spectrum is the region in the (ω, q) plane where it is possible for a photon with energy ω and momentum q to excite an electron-hole pair. This ability for pair creation is embodied in the polarization, in the regions where it has a nonzero imaginary part ($\mathrm{Im}[\Pi(\omega, q)] \neq 0$) (yellow regions shown in Fig. 2). It is worth noting that in all the frames of Fig. 2, the imaginary part of the polarization $[\mathrm{Im}\Pi(\omega, q)]$ can be divided into two disjunct regions by the parabolic boundary ($\omega \propto \beta q^2$). Meanwhile, the parabolic boundary ($\omega \propto \beta q^2$) parameter β become bigger as the hole concentration is increased.

While the imaginary part of the polarization determines the damping of the plasmon, the real part of the dynamical polarization comes in to determining the location of the plasmon branch in (ω, q) space. Therefore, we plot the real part of the polarization function $[\mathrm{Re}\Pi(\omega, q)]$ for hole-doped InSe and GaSe in Fig. 3, with hole concentrations chosen to correspond with Fig. 2.

From an experimental perspective, plasmons appear as resonance peaks in the momentum-resolved electron energy-loss spectrum, which directly measures the loss function: $\mathrm{Im}\varepsilon^{-1}(\omega, q)$. Here, we obtain the exact loss function by numerically integrating Eq. (6). The loss function for hole-doped InSe and GaSe is shown in Fig. 4 for carrier concentrations $n = 0.8 \times 10^{13}$ cm^{-2}, $n = 3.2 \times 10^{13}$ cm^{-2}, and $n = 5.6 \times 10^{13}$ cm^{-2} in Figs. 4(a)– 4(c) and 4(d)–4(f), respectively. In all the panels, there is a dominant plasmon peak

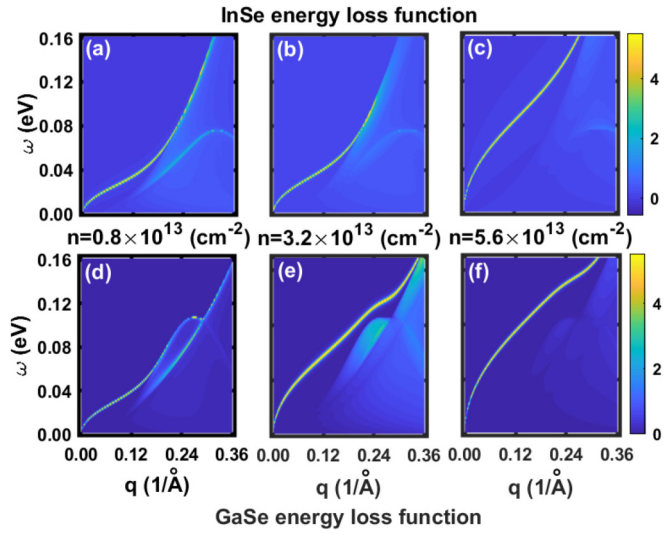

FIG. 4. Energy-loss function, $\mathrm{Im}\varepsilon^{-1}(\omega, q)$, for different carrier concentrations: (a) [(d)] $n = 8 \times 10^{12}$ cm^{-2}, (b) [(e)] $n = 32 \times 10^{12}$ cm^{-2}, and (c) [(f)] $n = 56 \times 10^{12}$ cm^{-2}, in hole-doped InSe [GaSe].

TABLE I. Numerical fitting parameters ω_0 in the formula $\omega = \omega_0\sqrt{q}$ for a hole-doped InSe monolayer with three kinds of carrier concentrations n under different environment dielectric constants ε_r.

	$n = 8 \times 10^{12}$ cm^{-2}	$n = 32 \times 10^{12}$ cm^{-2}	$n = 56 \times 10^{12}$ cm^{-2}
$\epsilon_r = 1$	$\omega_0 = 0.1986$	$\omega_0 = 0.4160$	$\omega_0 = 0.5278$
$\epsilon_r = 2$	$\omega_0 = 0.1406$	$\omega_0 = 0.2941$	$\omega_0 = 0.3726$
$\epsilon_r = 4$	$\omega_0 = 0.0999$	$\omega_0 = 0.2096$	$\omega_0 = 0.2633$

in the $\mathrm{Im}\Pi(\omega, q) = 0$ region, and it vanishes on entering the $\mathrm{Im}\Pi(\omega, q) \neq 0$ region, which is shown in Fig. 2.

In order to reconfirm the dependence between the plasmon energy and carrier density ($\omega_0 \propto \sqrt{n}$) revealed by Eq. (14), we explore the long-wavelength plasmon spectrum of hole-doped InSe based on the multiband Hamiltonian $\mathbf{H_{k\cdot p}}$ shown in Eq. (2). By using the numerical fitting method, we obtain the plasmon energy ω_0 under different carrier concentrations, as shown in Table I, and the corresponding plasmon spectrum is shown in Fig. 5. As we can see in Fig. 5, the hole-doped long-wavelength plasmon spectrum (solid lines in Fig. 5) can also be described using the conventional model $\omega = \omega_0\sqrt{q}$, where the constant ω_0 is determined by environment dielectric constant ε_r and carrier concentration n. When $q < 0.1/\text{Å}$, the RPA numerical results (dotted lines in Fig. 5) are in good agreement with the results (solid lines in Fig. 5) that are calculated using the analytical formula $\omega = \omega_0\sqrt{q}$. From the parameters shown in Table I, we conclude that the plasmon energy (ω_0) in hole-doped InSe is of the form $\omega_0 \propto \sqrt{n}/\sqrt{\varepsilon_r}$, which is consistent with the result shown in Eq. (14).

B. RPA results for electron-doping case

Since the conduction bands are parabolic, we can safely develop a single-band effective mass model $E_e(\mathbf{k}) = (\hbar^2/\mathbf{m}^*)\mathbf{k}^2 = \lambda\mathbf{k}^2$ to describe the electronic states near the conduction band minimum. Here, the parameter λ can easily be obtained by fitting the dispersion calculated using the single-band model with the electronic structure calculated by diagonalizing the multiband model given by Eq. (3). Here, we

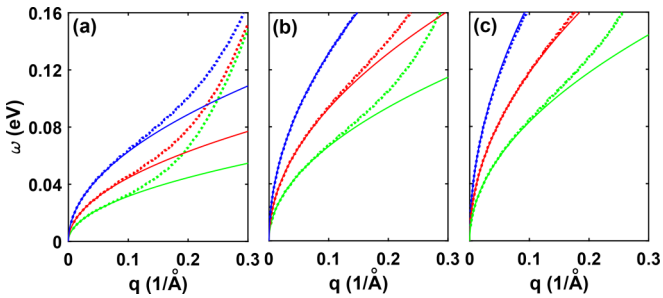

FIG. 5. Dotted lines show the hole-doped InSe plasmon spectrum calculated using the multiband $\mathbf{H_{k\cdot p}}$ Hamiltonian [Eq. (2)] for carrier concentrations (a) $n = 0.8 \times 10^{13}$ cm^{-2}, (b) $n = 3.2 \times 10^{13}$ cm^{-2}, and (c) $n = 5.6 \times 10^{13}$ cm^{-2}, by adopting different environment dielectric constants $\varepsilon_r = 1$ (green lines), $\varepsilon_r = 2$ (red lines), and $\varepsilon_r = 4$ (blue lines). The solid line is the numerical fitting results by adopting equation $\omega = \omega_0\sqrt{q}$.

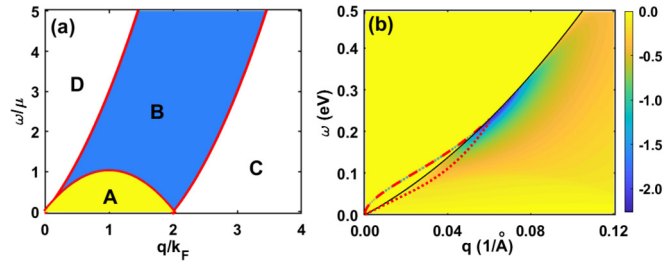

FIG. 6. (a) Regions with different expressions for the polarization function. At the borders, (k, ω) is the discontinuity of its derivative (red solid line). (b) Energy-loss function $(-\mathrm{Im}[\varepsilon(\omega, q)]^{-1})$ for electron doping the InSe monolayer, calculated using the analytical formulas given by Eq. (17) and Eq. (18). The red dashed (dotted) line stands for the undamped (damped) plasmon spectrum calculated using Eq. (20). The black line is the boundary between the B and D areas shown in (a), which can be described by the formula $\omega = \lambda q(q + 2k_F)$.

obtain the single-band parameter for the InSe (GaSe) monolayer: $\lambda = 18.8$ eV Å^2 ($\lambda = 20.8$ eV Å^2).

At first, we consider the imaginary part of Eq. (8),

$$\mathrm{Im}[\Pi(\omega, q)] = -\pi \int \frac{d^2k}{(2\pi)^2}\{f[E_e(\mathbf{k})] - f[E_e(\mathbf{k}+\mathbf{q})]\} \times \delta[\omega - E_e(\mathbf{k}+\mathbf{q}) + E_e(\mathbf{k})]. \quad (15)$$

Arguments of these δ functions determine the single-particle excitation (SPE) regions in the (k, ω) space. For an electron-doping case, with the Fermi energy located at μ and the Fermi wave vector $k_F = \sqrt{\mu/\lambda}$ [as shown in the green inset of Fig. 1(b)], we can analytically obtain the SPE regions shown in Fig. 6(a). The boundary between different regions can be described by different equations as below:

$$\begin{aligned} &A \in \{\omega < \lambda q(2k_F - q)\}, \\ &B \in \{\omega > \lambda q(2k_F - q) \cap \omega < \lambda q(q + 2k_F) \cap \omega > \lambda q(q - 2k_F)\}, \\ &C \in \{\omega < \lambda q(q - 2k_F)\}, \\ &D \in \{\omega > \lambda q(q + 2k_F)\}. \end{aligned} \quad (16)$$

As we can see in Fig. 6(a), the imaginary part of the polarization function $\mathrm{Im}[\Pi(\omega, q)] == 0$ in the white space (regions C and D). Region B in Fig. 6(a) corresponds to regions in which collective oscillations are damped.

After the tedious but straightforward integration of Eq. (15), we obtain the imaginary part of the polarization function as

$$\mathrm{Im}[\Pi(\omega, q)] = \frac{1}{4\pi\lambda q}\left[M_+\sqrt{k_F^2 - \left(\frac{\omega + \lambda q^2}{2\lambda q}\right)^2} - M_-\sqrt{k_F^2 - \left(\frac{\omega - \lambda q^2}{2\lambda q}\right)^2}\right]. \quad (17)$$

By substituting this result [Eq. (17)] into Eq. (7), we can get the real part of the polarization function as

$$\mathrm{Re}[\Pi(\omega, q)] = -\frac{1}{4\pi\lambda q}\left[q - R_+\sqrt{\left(\frac{\omega + \lambda q^2}{2\lambda q}\right)^2 - k_F^2}\right.$$

$$- R_{-}\sqrt{\left(\frac{\omega-\lambda q^2}{2\lambda q}\right)^2 - k_F^2}\Bigg], \tag{18}$$

where

$$\begin{aligned} A &\to \{R_+ = 0, R_- = 0, M_+ = 1, M_- = 1\}, \\ B &\to \{R_+ = 1, R_- = 0, M_+ = 0, M_- = 1\}, \\ C &\to \{R_+ = 1, R_- = 1, M_+ = 0, M_- = 0\}, \\ D &\to \{R_+ = 1, R_- = -1, M_+ = 0, M_- = 0\}. \end{aligned} \tag{19}$$

The plasmon branch can be obtained by finding the zeros of the dielectric function $\epsilon(\omega - i\tau, q)$, where τ is the plasmon decay rate. It is sufficient to get the plasmon dispersion by solving $q = e^2/(2\epsilon_0\epsilon_r)\mathrm{Re}\Pi(\omega, q)$ in region D. Here, we analytically obtain the plasmon dispersion as

$$\begin{aligned} &\text{Region D: } \omega_q = \frac{(\lambda q + \alpha)\sqrt{\lambda q(\lambda^2 q^4 + 2\alpha\lambda q^3 + 4\alpha^2 k_F^2)}}{\alpha\sqrt{\lambda q + 2\alpha}}, \\ &\text{Region B: } \omega_q = \lambda q[2\sqrt{(\lambda q^2/\alpha + q)^2 + k_F^2} - q], \end{aligned} \tag{20}$$

where $\alpha = e^2/(8\pi\varepsilon_0\varepsilon_r)$.

In the framework of RPA, the plasmon dispersion $\omega_p(q)$ can also be given by the poles of the loss function, $\mathrm{Im}[\varepsilon(\omega, q)]^{-1}$. This function is calculated using Eqs. (17) and (18) for electron-doping strength $n = 0.8 \times 10^{13}$ cm^{-2} and the calculation result is plotted in Fig. 6(b). It is worth noting that the plasmon spectrum [red dashed line in Fig. 6(b)], calculated using the analytical result shown in Eq. (20), is in very good agreement with the poles of the loss function, $-\mathrm{Im}[\varepsilon(\omega, q)]^{-1}$ [blue dotted line in Fig. 6(b)]. For the damped plasmon [dotted red line in Fig. 6(b)], the damping rate can be calculated by

$$\begin{aligned} \tau &= \frac{\mathrm{Im}[\Pi(\omega, q)]}{\partial\mathrm{Re}[\Pi(\omega, q)]\partial\omega} \\ &= \frac{2\lambda q(\lambda q^2/\alpha + q)\sqrt{k_F^2 - [\sqrt{(\lambda q^2/\alpha + q)^2 + k_F^2} - q]^2}}{\sqrt{(\lambda q^2/\alpha + q)^2 + k_F^2}}. \end{aligned} \tag{21}$$

The above analysis for the electron-doping case is based on the single parabolic band model. When the Fermi energy is located near the conduction band minimum, the results generated by the parabolic band model can describe the dielectric properties very well. However, the electronic structure, which is far away from the conduction band minimum, cannot be described by the single parabolic band model very well. Therefore, we recalculate the polarization function by using the multiband Hamiltonian shown in Eq. (3).

We numerically calculate the imaginary part of the polarization function shown in Fig. 7, where we plot the $\mathrm{Im}\Pi(\omega, q)$ for the electron-doped InSe and GaSe monolayer on the top and bottom rows. As we can see in Fig. 7, the imaginary part of the polarization $[\mathrm{Im}\Pi(\omega, q)]$ can be divided into two disjunct regions where the intraband electron-hole pair formation is impossible $[\mathrm{Im}\Pi(\omega, q) = 0]$ or possible $[\mathrm{Im}\Pi(\omega, q) \neq 0]$

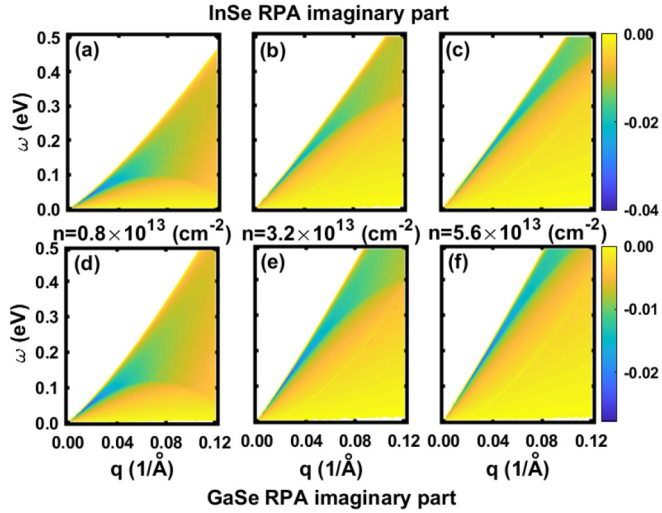

FIG. 7. Imaginary part of the polarization function, $\mathrm{Im}[\Pi(\omega, q)]$, for different carrier concentrations: (a) [(d)] $n = 8 \times 10^{12}$ cm^{-2}, (b) [(e)] $n = 32 \times 10^{12}$ cm^{-2}, and (c) [(f)] $n = 56 \times 10^{12}$ cm^{-2}, in electron-doped InSe [GaSe].

by the line boundary. These numerical results for electron doping are consistent with the analytical results obtained by using the single-band parabolic model where the boundary $[\omega \propto q(q + 2k_F)$ shown in Fig. 6(a)] approaches the linear relation $\omega \propto 2k_F q$ for small q. As the electron concentration is increased from $n = 8 \times 10^{12}$ cm^{-2} [Figs. 7(a) and 7(d)] to $n = 56 \times 10^{12}$ cm^{-2} [Figs. 7(c) and 7(f)], the slope of the linear boundary increases. This is because the higher electron concentration tunes up the Fermi energy, which leads to a bigger Fermi wave vector k_F in the formula ($\omega \propto 2k_F q$).

$\mathrm{Re}\Pi(\omega, q)$ is plotted in Fig. 8 with the electron concentration chosen to correspond to Fig. 7. As we can see in Fig. 8, the real part of the polarization $[\mathrm{Re}\Pi(\omega, q)]$ can be divided into different regions, as shown in Fig. 7, and the

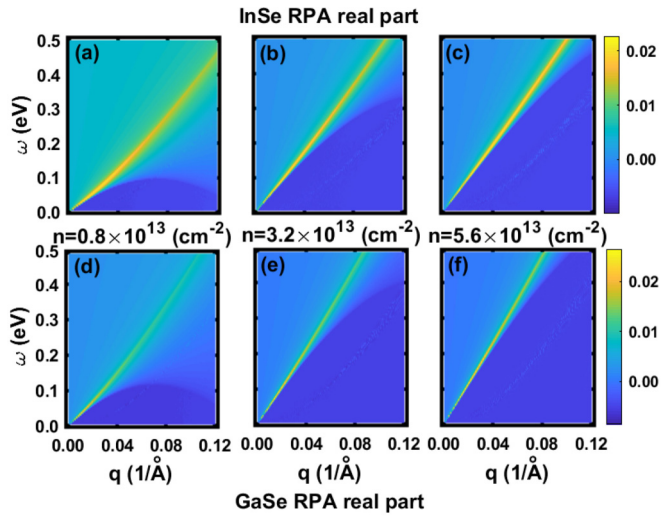

FIG. 8. Real part of the polarization function, $\mathrm{Re}[\Pi(\omega, q)]$, for different carrier concentrations: (a) [(d)] $n = 8 \times 10^{12}$ cm^{-2}, (b) [(e)] $n = 32 \times 10^{12}$ cm^{-2}, and (c) [(f)] $n = 56 \times 10^{12}$ cm^{-2}, in electron-doped InSe [GaSe].

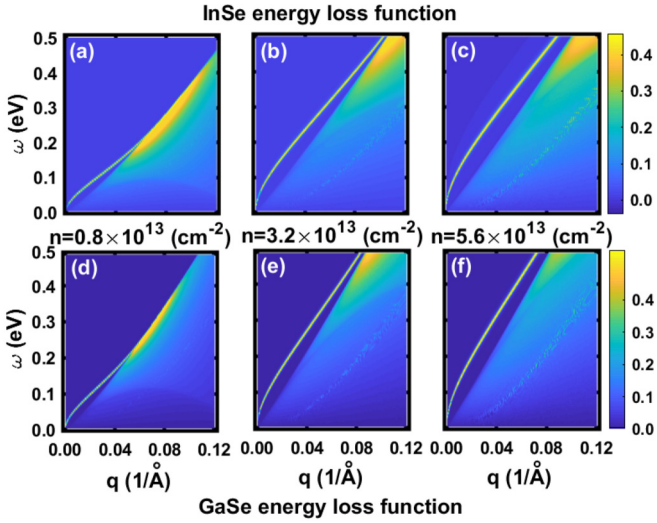

FIG. 9. Energy-loss function, $\mathrm{Im}[\varepsilon^{-1}(\omega, q)]$, for different carrier concentrations: (a) [(d)] $n = 8 \times 10^{12}$ cm^{-2}, (b) [(e)] $n = 32 \times 10^{12}$ cm^{-2}, and (c) [(f)] $n = 56 \times 10^{12}$ cm^{-2}, in electron-doped InSe [GaSe].

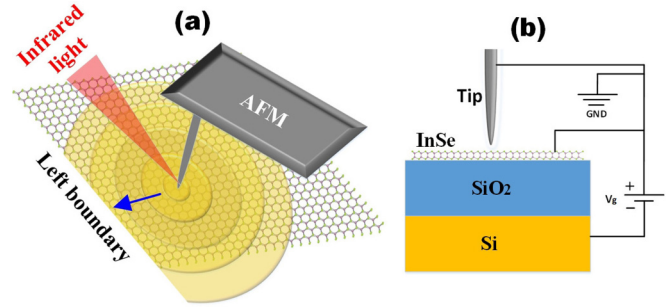

FIG. 10. (a) Diagram of an infrared nanoimaging experiment. The red triangle displays the incident infrared light. Concentric yellow circles illustrate plasmon waves launched by the illuminated atomic force microscope (AFM) tip. (b) The gate bias setup. Both the metalized tip and InSe monolayer are at the ground (GND) potential.

real part of the polarization $[\mathrm{Re}\Pi(\omega, q)]$ plotted in Fig. 8 is equal to a constant in a small ω region. These numerical results can by explained by the analytical results [Eq. (18)], where $\mathrm{Re}\Pi(\omega, q) = -1/(4\pi\lambda)$ in region A: $\omega < \lambda q(2k_F - q)$. As the electron concentration is increased from $n = 8 \times 10^{12}$ cm^{-2} [Figs. 8(a) and 8(d)] to $n = 56 \times 10^{12}$ cm^{-2} [Figs. 8(c) and 8(f)], the constant $\mathrm{Re}\Pi(\omega, q)$ region becomes bigger. This is because the higher electron concentration tunes up the Fermi energy, which leads to a bigger Fermi wave vector k_F in the formula $[\omega < \lambda q(2k_F - q)]$. It is worth noting that in Figs. 7 and 8, the GaSe imaginary $[\mathrm{Im}\Pi(\omega, q)]$ and real $[\mathrm{Re}\Pi(\omega, q)]$ parts of the polarization have similar characteristics as the InSe results.

Next, we also obtain the energy-loss function by using the multiband Hamiltonian shown in Eq. (3). The energy-loss function for electron-doped InSe and GaSe is shown in Fig. 9 for carrier concentrations $n = 0.8 \times 10^{13}$ cm^{-2}, $n = 3.2 \times 10^{13}$ cm^{-2}, $n = 5.6 \times 10^{13}$ cm^{-2} in Figs. 9(a)–9(c) and Figs. 9(d)– 9(f), respectively. In all the panels, there is a dominant plasmon peak in the region $\mathrm{Im}\Pi(\omega, q) = 0$, and it vanishes on entering the intraband particle hole continuum, whose boundary is also doping dependent, as shown in Fig. 7. Since the structure of the valence bands is quite different compared to the conduction bands, the plasmon dispersions (energy-loss resonance peak) for the electron-doping case (shown in Fig. 9) clearly differ from the hole-doping case shown in Fig. 4, where ω is energetically higher in the electron-doped XSe (X = In, Ga) under the same doping strength (n).

From Fig. 9, one can furthermore see that the long-wavelength plasmon energy in electron-doped XSe (X = In, Ga) is of the form $\omega \propto \sqrt{n}\sqrt{q}$, which is the same as the form in 2DEGs. This can be understood from the long-wavelength behavior of Eq. (20). Under the long-wavelength limit ($q \to 0$), Eq. (20) can be simplified to $\omega \propto \omega_0\sqrt{q} \propto (\sqrt{\lambda}\sqrt{n}/\sqrt{\epsilon_r})\sqrt{q} \propto (\sqrt{\mu}/\sqrt{\epsilon_r})\sqrt{q}$. Here, μ stands for Fermi energy with the zero Fermi energy located at the conduction band minimum and n represents the electron concentration. Therefore, the plasmon energy ω_0 relies on $\sqrt{n}$ for the electron-doped monolayer XSe (X = In, Ga).

IV. EXPERIMENT SETUP DISCUSSION

Plasmons in 2D materials can be accessed by a variety of direct and indirect methods, including optical measurements, electron energy-loss spectroscopy (EELS), inelastic light scattering, angle-resolved photoemission spectroscopy (ARPES), and scanning tunneling spectroscopy [4,31,32]. Here, we introduce an experimental method which can be used to observe the dependence between the Fermi energy and the plasmon wavelength.

One can use the scattering-type scanning near-field optical microscope (scattering-type SNOM) to experimentally excite a plasmon wave by illuminating the sharp tip of an atomic force microscope (AFM) with a focused infrared beam [Fig. 10(a)]. The momenta imparted by the tip extend up to a few times $1/a$, where $a < 25$ nm is the curvature radius of the tip, thus spanning the typical range of infrared plasmon momenta in the InSe monolayer. As we can see in Fig. 10(a), illuminated by focused infrared light, the AFM tip launches plasmon waves (yellow concentric circles) propagating radially outward from the tip. The left boundary shown in Fig. 10(a) acts as reflectors of the plasmon waves, directing them back to the tip. Therefore, complex patterns of interference between the launched and reflected plasmons should form inside InSe. As the tip is scanned towards the left boundary along the blue arrow in Fig. 10(a), it registers these plasmon formed standing-wave oscillations with periodicity given by $\lambda/2$, where λ is the plasmon wavelength.

The above phenomena can be readily manipulated with gate voltage, which changes both the carrier concentration and Fermi energy in 2D materials. In graphene, gating with a solid electrolyte allowed carrier concentrations as large as 10^{14} cm^{-2} to be achieved, which increases the Fermi energy into 1 eV, such that the plasmon wavelength can be tuned into infrared [33]. In the InSe monolayer, the carrier concentration and Fermi energy can also be tuned as in graphene. The corresponding experiment setup is shown in Fig. 10(b).

V. CONCLUSION

We have investigated the dynamical dielectric function in monolayer InSe and GaSe. We find that although the monolayer *X*Se (*X*=In,Ga) has a nonparabolic "Mexican hat" topmost valence band dispersion which is so different from the parabolic band structure in 2DEGs, the corresponding density dependence of the plasmon energy is still of the form $\omega_0 \propto \sqrt{n}$ (n is the carrier concentration) as in 2DEGs. However, the Mexican hat topmost valence band leads to a special dependence between Fermi energy $|\mu|$ and carrier concentration n as the form $n \propto \sqrt{|\mu|}$. Therefore, the dependence between the Fermi energy $|\mu|$ and plasmon energy ω_0 is of the form $\omega_0 \propto |\mu|^{1/4}$ for the hole-doped monolayer *X*Se (X = In, Ga).

[1] M. Pletyukhov and V. Gritsev, Phys. Rev. B **74**, 045307 (2006).
[2] C. A. Ullrich and M. E. Flatté, Phys. Rev. B **68**, 235310 (2003).
[3] J. Schliemann, Phys. Rev. B **74**, 045214 (2006).
[4] K. N. A. Grigorenko, M. Polini, Nat. Photon. **6**, 749 (2012).
[5] M. Benaissa, W. Sigle, M. Korytov, J. Brault, P. Vennéguès, and P. A. van Aken, Appl. Phys. Lett. **103**, 021901 (2013).
[6] R. H. Ritchie, Phys. Rev. **106**, 874 (1957).
[7] R. A. Ferrell, Phys. Rev. **111**, 1214 (1958).
[8] F. Stern, Phys. Rev. Lett. **18**, 546 (1967).
[9] C. C. Grimes and G. Adams, Phys. Rev. Lett. **36**, 145 (1976).
[10] M.-T. Bootsmann, C.-M. Hu, C. Heyn, D. Heitmann, and C. Schüller, Phys. Rev. B **67**, 121309(R) (2003).
[11] M.-l. Ke, D. Westwood, R. H. Williams, and M. J. Godfrey, Phys. Rev. B **51**, 5038 (1995).
[12] J. Seidel, F. I. Baida, L. Bischoff, B. Guizal, S. Grafström, D. Van Labeke, and L. M. Eng, Phys. Rev. B **69**, 121405(R) (2004).
[13] K. Seal, D. A. Genov, A. K. Sarychev, H. Noh, V. M. Shalaev, Z. C. Ying, X. Zhang, and H. Cao, Phys. Rev. Lett. **97**, 206103 (2006).
[14] V. N. Konopsky and E. V. Alieva, Phys. Rev. Lett. **97**, 253904 (2006).
[15] W. H. Weber, Phys. Rev. Lett. **39**, 153 (1977).
[16] V. I. Safarov, V. A. Kosobukin, C. Hermann, G. Lampel, J. Peretti, and C. Marlière, Phys. Rev. Lett. **73**, 3584 (1994).
[17] A. H. Castro Neto, F. Guinea, N. M. R. Peres, K. S. Novoselov, and A. K. Geim, Rev. Mod. Phys. **81**, 109 (2009).
[18] E. H. Hwang and S. Das Sarma, Phys. Rev. B **75**, 205418 (2007).
[19] V. W. Brar, S. Wickenburg, M. Panlasigui, C.-H. Park, T. O. Wehling, Y. Zhang, R. Decker, i. m. c. b. u. Girit, A. V. Balatsky, S. G. Louie, A. Zettl, and M. F. Crommie, Phys. Rev. Lett. **104**, 036805 (2010).
[20] C. J. Tabert and E. J. Nicol, Phys. Rev. B **89**, 195410 (2014).
[21] A. Scholz, T. Stauber, and J. Schliemann, Phys. Rev. B **88**, 035135 (2013).
[22] D. J. Late, B. Liu, J. Luo, A. Yan, H. S. S. R. Matte, M. Grayson, C. N. R. Rao, and V. P. Dravid, Adv. Mater. **24**, 3549 (2012).
[23] A. K. G. V. I. Fal'ko and Y. Cao, Nat. Nanotechnol. **12**, 223 (2017).
[24] V. Zólyomi, N. D. Drummond, and V. I. Fal'ko, Phys. Rev. B **87**, 195403 (2013).
[25] D. V. Rybkovskiy, A. V. Osadchy, and E. D. Obraztsova, Phys. Rev. B **90**, 235302 (2014).
[26] M. Zhou, S. Yu, W. Yang, W.-k. Lou, F. Cheng, D. Zhang, and K. Chang, Phys. Rev. B **100**, 245409 (2019).
[27] M. Zhou, D. Zhang, S. Yu, Z. Huang, Y. Chen, W. Yang, and K. Chang, Phys. Rev. B **99**, 155402 (2019).
[28] M. Zhou, R. Zhang, J. Sun, W.-K. Lou, D. Zhang, W. Yang, and K. Chang, Phys. Rev. B **96**, 155430 (2017).
[29] Y. Yoon, K. Ganapathi, and S. Salahuddin, Nano Lett. **11**, 3768 (2011).
[30] M.-W. Lin, L. Liu, Q. Lan, X. Tan, K. S. Dhindsa, P. Zeng, V. M. Naik, M. M.-C. Cheng, and Z. Zhou, J. Phys. D **45**, 345102 (2012).
[31] T. Eberlein, U. Bangert, R. R. Nair, R. Jones, M. Gass, A. L. Bleloch, K. S. Novoselov, A. Geim, and P. R. Briddon, Phys. Rev. B **77**, 233406 (2008).
[32] Y. Liu, R. F. Willis, K. V. Emtsev, and T. Seyller, Phys. Rev. B **78**, 201403(R) (2008).
[33] Z. Fei, A. S. Rodin, G. O. Andreev, W. Bao, A. S. McLeod, M. Wagner, L. M. Zhang, Z. Zhao, M. Thiemens, G. Dominguez, M. M. Fogler, A. H. Castro Neto, C. N. Lau, F. Keilmann, and D. N. Basov, Nature (London) **487**, 82 (2012).